ACS NANO

www.acsnano.org

ARTICLE

# Nickel-Laden Dendritic Plasmonic Colloidosomes of Black Gold: Forced Plasmon Mediated Photocatalytic $CO_2$ Hydrogenation

Rishi Verma, Rajesh Belgamwar, Pratip Chatterjee, Robert Bericat-Vadell, Jacinto Sa, and Vivek Polshettiwar*

Cite This: *ACS Nano* 2023, 17, 4526–4538

Read Online

ACCESS | Metrics & More | Article Recommendations | Supporting Information

**ABSTRACT:** In this work, we have designed and synthesized nickel-laden dendritic plasmonic colloidosomes of Au (black gold-Ni). The photocatalytic $CO_2$ hydrogenation activities of black gold-Ni increased dramatically to the extent that measurable photoactivity was only observed with the black gold-Ni catalyst, with a very high photocatalytic CO production rate (2464 ± 40 mmol $g_{Ni}^{-1}$ $h^{-1}$) and 95% selectivity. Notably, the reaction was carried out in a flow reactor at low temperature and atmospheric pressure without external heating. The catalyst was stable for at least 100 h. Ultrafast transient absorption spectroscopy studies indicated indirect hot-electron transfer from the black gold to Ni in less than 100 fs, corroborated by a reduction in Au−plasmon electron−phonon lifetime and a bleach signal associated with Ni d-band filling. Photocatalytic reaction rates on excited black gold-Ni showed a superlinear power law dependence on the light intensity, with a power law exponent of 5.6, while photocatalytic quantum efficiencies increased with an increase in light intensity and reaction temperature, which indicated the hot-electron-mediated mechanism. The kinetic isotope effect (KIE) in light (1.91) was higher than that in the dark (~1), which further indicated the electron-driven plasmonic $CO_2$ hydrogenation. Black gold-Ni catalyzed $CO_2$ hydrogenation in the presence of an electron-accepting molecule, methyl-*p*-benzoquinone, reduced the CO production rate, asserting the hot-electron-mediated mechanism. Operando diffuse reflectance infrared Fourier transform spectroscopy (DRIFTS) showed that $CO_2$ hydrogenation took place by a direct dissociation path via linearly bonded Ni−CO intermediates. The outstanding catalytic performance of black gold-Ni may provide a way to develop plasmonic catalysts for $CO_2$ reduction and other catalytic processes using black gold.

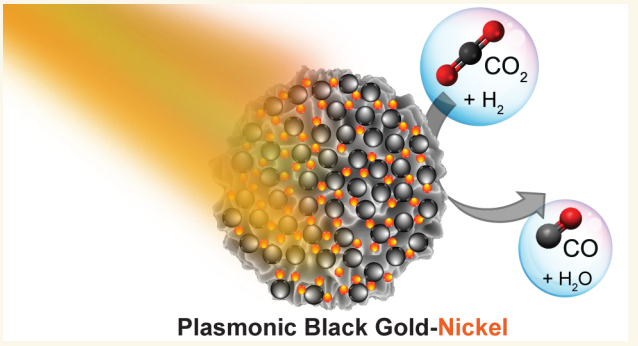


**KEYWORDS:** *carbon dioxide fixation, $CO_2$ hydrogenation, plasmonic catalysis, photocatalysis, photochemistry*



## INTRODUCTION

$CO_2$ valorization processes are crucial to mitigate global warming and combat climate change. The production of chemicals and fuels via the hydrogenation of $CO_2$ by green hydrogen is one of the promising paths for mitigating $CO_2$ emissions.[1−3] Transforming $CO_2$ into useful chemicals, using green hydrogen, not only utilizes $CO_2$ but also reduces the use of fossil-derived carbon materials. $CO_2$ hydrogenation is a challenging process due to the thermodynamic stability of $CO_2$ molecule, making the overall process unsustainable. However, excellent progress has been made toward converting $CO_2$ to various products via hydrogen reduction using thermo-, photo-, and electrochemical ways.[4−6] The heterogeneous photocatalytic reaction of $CO_2$ and green hydrogen under atmospheric pressure produces different valuable chemicals.[7−10]

$CO_2$ hydrogenation with green hydrogen can provide a single solution to three challenging problems: (i) excessive $CO_2$ levels, (ii) the temporal mismatch between solar electricity production and demand, and (iii) hydrogen gas storage.[11−13] However, the $CO_2$ hydrogenation reaction needs very high temperatures, causing quick deactivation of the

Received: October 20, 2022
Accepted: February 7, 2023
Published: February 13, 2023

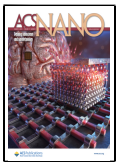

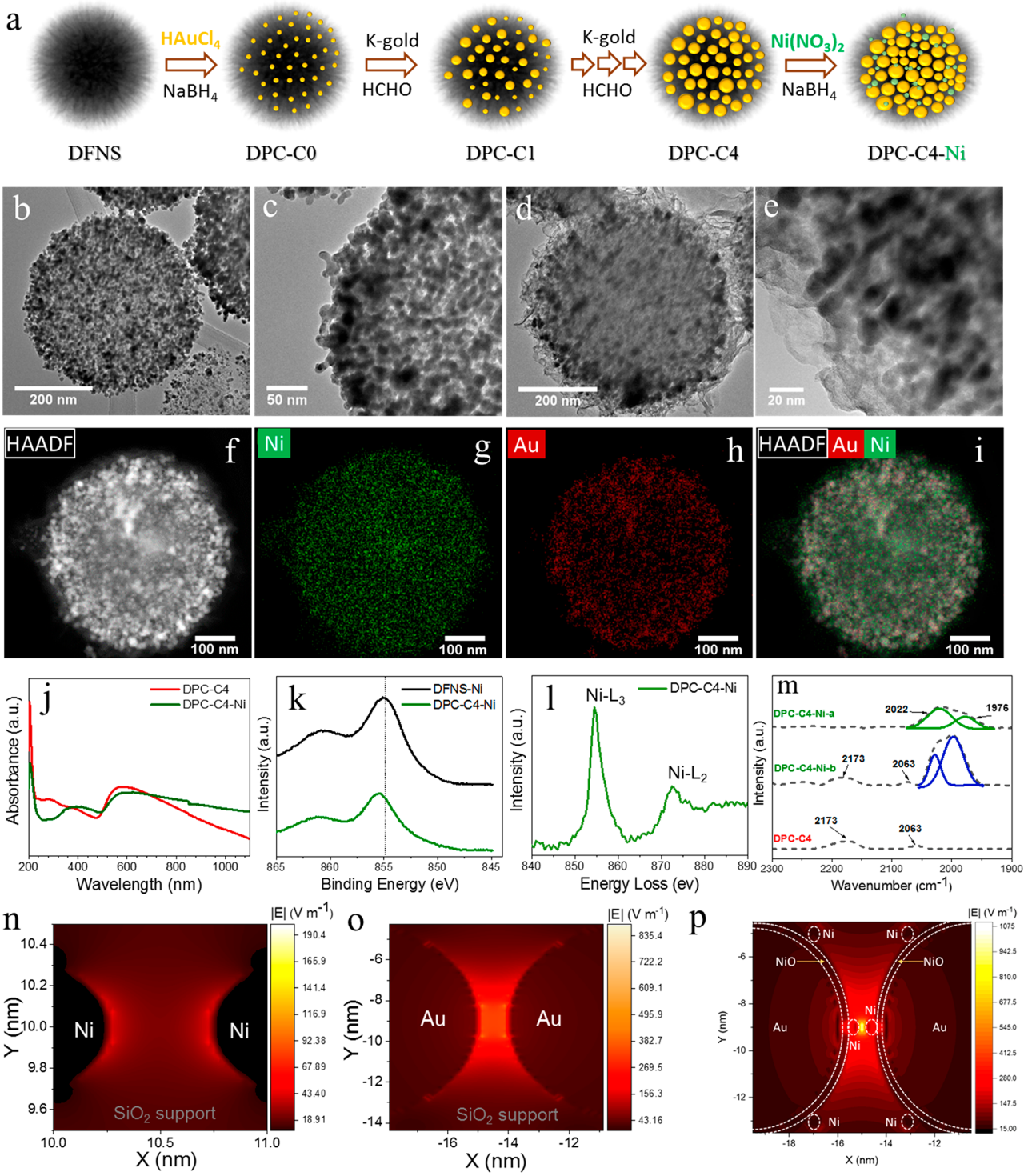


**Figure 1. (a) Schematic illustration of the synthesis process of DPC-C4-Ni. TEM images of (b, c) DPC-C4 and (d, e) DPC-C4-Ni. (f–i) STEM-EDS elemental mapping of DPC-C4-Ni. (j) UV-DRS spectrum of DPC-C4 and DPC-C4-Ni (after subtraction of scattering due to DFNS). (k) Ni 2p XPS spectra expanded in the region of Ni $2p_{3/2}$. (l) EELS specttum of DPC-C4-Ni. (m) DRIFT spectra of CO adsorbed on DPC-C4 (bottom) and DPC-C4-Ni (a after purging and b before purging by argon gas). Electric field intensities (V $m^{-1}$) in (n) DFNS-Ni, (o) DPC-C4, and (p) DPC-C4-Ni, using FDTD simulation.**

catalyst due to active site sintering and coke formation. We, therefore, asked this question: can this high-temperature reaction be catalyzed at room to moderate temperature via plasmonic excitation of $H_2$ and $CO_2$ using a plasmonic catalyst?

Plasmonic nanocatalysts are a paradigm in heterogeneous photocatalysis.[14−21] Localized surface plasmon resonance (LSPR) damping generates hot carriers as well as localized heating in plasmonic nanoparticles, which then interact with reactant molecules and activate their chemical bonds.[22−29] A hybrid catalyst design in which plasmonic metal undergoes



https://doi.org/10.1021/acsnano.2c10470
ACS Nano 2023, 17, 4526−4538

LSPR and induces optical polarization in a nonplasmonic metal in its vicinity (known as forced plasmon) is another innovative way to broaden the scope of plasmonic catalysis in a variety of reactions.[30−35]

In this work, we have designed dendritic plasmonic colloidosomes of Au loaded with nickel sites (DPC-C4-Ni), prepared by loading four cycles of Au NPs on dendritic fibrous nanosilica (DFNS).[36−40] The choice of nickel was inspired by its exceptional activities for thermal $CO_2$ hydrogenation. DPC-C4-Ni absorbs broad-band light of the solar spectrum and produces intense localized hot spots. When DPC-C4-Ni was illuminated with visible light, it became highly catalytically active, and it was able to catalyze $CO_2$ hydrogenation using solar light. The $CO_2$ hydrogenation reaction mechanism was studied by using (i) finite-difference time-domain simulations (FDTD), (ii) light-intensity-dependent production rate, (iii) light-intensity-dependent photocatalytic quantum efficiencies, (iv) wavelength-dependent production rate, (v) kinetic isotope effect (KIE), (vi) ultrafast transient absorption spectroscopy, and (vii) *in situ* diffuse reflectance infrared Fourier transform spectroscopy (DRIFTS).

## RESULTS AND DISCUSSION

**Synthesis and Characterization of Dendritic Plasmonic Colloidosome (Black Gold) Ni Catalyst.** Conventional plasmonic nanocatalysts have intense absorptions but are narrow.[14−21] In this work, we have designed and synthesized dendritic plasmonic colloidosomes of Au (black gold), based on a nickel photocatalyst that absorbs across the entire visible to NIR range.

This was achieved by a high loading of Au with control over gaps between Au nanoparticles (NPs) on the DFNS[36−40] support without significantly reducing its surface area and porosity. The DFNS sheet's open fibrous morphology allowed the deposition of Au NPs with controllable gaps between them. Four cycle-by-cycle growth steps were needed to prepare black gold (DPC-C4) having a good surface area with broad-band light absorption. DPC-C4-Ni was prepared by Ni deposition and hydrogen reduction (Figure 1a). A transmission electron microscopy (TEM) analysis of DPC-C4 indicates a uniform coating of Au NPs on DFNS (Figures 1b,c and Figure S1) having an average particle size of 9.5 nm, distributed across the DFNS spheres of ∼500 nm. In the case of DPC-C4-Ni, a thin coating of amorphous nickel oxide on DPC-C4 was observed, onto which small Ni NPs (1−4 nm) were loaded (Figure 1d,e and Figures S2−S8). In scanning transmission electron microscopy high-angle annular dark-field (STEM-HAADF) images of DPC-C4-Ni, the poor contrast between the Au and Ni posed a challenge in exactly locating the small Ni NPs on Au NPs (Figures S3 and S4). However, point scanning transmission electron microscopy (STEM) with energy-dispersive X-ray spectroscopy (EDS) was able to distinguish Au NPs from the small Ni NPs loaded on Au (Figures S5 and S6). STEM-EDS elemental mapping of DPC-C4-Ni indicated the uniform loading of Ni across DPC-C4 spheres (Figure 1f−i and Figure S7). The ultramicrotome samples of DPC-C4-Ni (Figure S8) also indicated the uniform loading of Au and Ni nanoparticles at different cross-sections of the silica nanospheres. Powder X-ray diffraction (PXRD) patterns of DPC-C4 indicated the formation of $Au^0$ NPs (Figure S9). PXRD of DPC-C4-Ni also did not show any peaks for Ni (Figure S9), indicating the amorphous state of nickel oxide and the small size of Ni NPs. Elemental analysis indicated that DPC-C4 has an Au loading of 51.3 ± 4.7 wt %, while DPC-C4-Ni has 46.8 ± 2.2 wt % of Au and 9.2 ± 2.1 wt % of Ni. The Ni loading in DPC-C4-Ni was also found to be 9.6 ± 0.9% by ICP-MS.

Plasmonic coupling and heterogeneity in Au NPs resulted in black DPC-C4 (hence named black gold), due to broad-band light absorption in the visible region (Figure 1j). An $N_2$ sorption analysis indicated a decrease in surface area of DPC-C4-Ni to 175 $m^2\ g^{-1}$ (from 214 $m^2\ g^{-1}$ for DPC-C4), while the pore volume decreased to 0.19 $cm^3\ g^{-1}$ (from 0.31 $cm^3\ g^{-1}$ of DPC-C4) (Figure S10). This reduction in porosity was expected due to the coating of Ni species on DPC-C4. For control experiments, DFNS-Ni was also synthesized by reducing nickel nitrate on DFNS (Figure S11).

In an X-ray photoelectron spectroscopy (XPS) analysis (Figure 1k and Figure S12), the binding energy (BE) of 84 eV for Au $4f_{7/2}$ was consistent with the $Au^0$ oxidation state (Figure S12). The Ni 2p spectrum of DPC-C4-Ni showed a Ni $2p_{3/2}$ binding energy of 855.4 eV (Figure 1k), indicating the presence of amorphous nickel oxide.[41] STEM with electron energy loss spectroscopy (EELS) showed the Ni $L_3$ and $L_2$ edges, which represented the Ni 2p → Ni 3d electron transition and directly probed the Ni 3d orbital occupancy (Figure 1l), which also indicated the oxidized state of Ni. To further probe the electronic state of nickel sites, a CO adsorption followed by a DRIFTS study was then carried out (Figure 1m). The spectra before argon (Ar) purging had signals corresponding to CO adsorbed atop Au at 2063 $cm^{-1}$ and on low-coordinated Au sites at 2173 $cm^{-1}$ in DPC-C4 and DPC-C4-Ni.[42,43] However, after purging the catalyst with argon gas for 6 min (details in the Experimental Section in the Supporting Information), the signals coming from Au sites were reduced. This was because the plasmon excitation was providing energy to desorb weakly bound CO from Au NPs as compared to Ni NPs.[35] The DRIFT spectra after argon purging showed CO adsorbed on DPC-C4-Ni with two bands centered at 2022 and 1976 $cm^{-1}$ assigned to CO molecules adsorbed on $Ni^0$ ultrasmall nanoparticles with linear and bridge orientations, respectively.[44] This indicated the stronger binding of CO on active Ni sites as compared to Au sites in the presence of light.

FDTD simulations of DPC-C4-Ni (where DPC-C4 was coated with a thin layer of nickel oxide) were carried out to study the role of elevated electric fields (Figure 1n−p and Figure S13). The electric field distribution under light excitation in DFNS-Ni ($E$ = 23 V $m^{-1}$, at the center of the gap) was weak (Figure 1n), because the plasmon resonance of Ni NPs falls in the UV range. The electric field distribution in the case of DPC-C4 ($E$ = 334 V $m^{-1}$) was high due to the LSPR of gold nanoparticles under visible-light irradiation (Figure 1o). Notably, the calculated electric field was significantly elevated in the case of DPC-C4-Ni ($E$ = 1074 V $m^{-1}$), 47 times more than in DFNS-Ni, which can be attributed to the near-field coupling between the Ni and Au nanoparticles. The electric field was mainly concentrated around Ni sites within the gaps of Au NPs (Figure 1p). This elevated electric field can play a crucial role in the activation of chemical bonds.[27,29] We conducted photoluminescence (PL) studies of methylene blue (MB) dye in the presence and absence of DPC-C4 or DPC-C4-Ni to further investigate the effect of the enhanced electric field. After being excited by a 630 nm laser, pure MB emits a broad-band emission centered around 760 nm (Figure S14). The presence of DPC-C4 and


https://doi.org/10.1021/acsnano.2c10470
ACS Nano 2023, 17, 4526−4538

DPC-C4-Ni, in particular, increased MB emission by a factor of 2.4. (Figure S14). The high electric field excites more MB dye molecules, resulting in more emissions after the molecules are relaxed to the ground state.[45] DPC-C4 and DPC-C4-Ni did not exhibit a strong PL; hence, their contribution to the emission spectra of MB adsorbed on their surfaces was marginal (Figure S14).

**Plasmonic $H_2/D_2$ Dissociation.** We explored the DPC-C4-Ni catalyst for $H_2/D_2$ dissociation, which is a key step toward the $CO_2$ hydrogenation reaction (Figure 2). When it

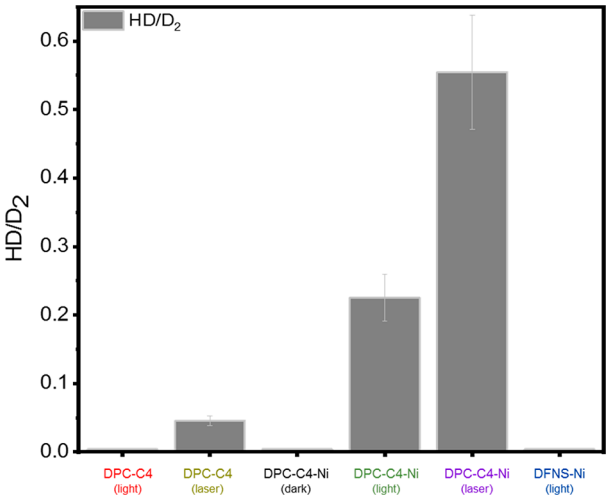


**Figure 2. Plasmon-induced $H_2/D_2$ dissociation and formation of HD. Light: xenon lamp (400−1100 nm, 0.78 W $cm^{-2}$). Laser: supercontinuum broad-band laser (400−2500 nm, 21.2 W $cm^{-2}$).**

was exposed to light, DPC-C4 showed no catalytic activity, whereas DPC-C4-Ni showed a good amount of HD formation (Figure 2). The temperature of the catalyst bed was measured by inserting a thin thermocouple inside the bed (direct contact with the catalyst powder), and it was found to be 50 °C, as we used a visible-light source (not a laser). The dark experiment at 50 °C using DPC-C4-Ni showed no HD formation (Figure 2).

When the xenon lamp was replaced by a a high-power white-light laser, DPC-C4-Ni showed greater HD formation (Figure 2). This power-dependence increase in activity indicates the role of plasmonic excitation in catalysis. The significant increase in HD formation by DPC-C4-Ni compared to DPC-C4 and DFNS-Ni also suggested the involvement of charge carriers of Ni sites.[46] Nickel nanoparticles were also reported to show LSPR in the visible region, although for a particle size of around 100 nm.[47] For smaller Ni NPs, their LSPR was in the UV range.[48] In DPC-C4-Ni catalysts, Ni NPs are small (1−4 nm) and hence Ni NPs alone (without DPC-C4) did not show any LSPR or optical excitation in the visible region.

**Plasmonic $CO_2$ Hydrogenation.** We explored DPC-C4-Ni for photocatalytic $CO_2$ hydrogenation (Figure 3). The plasmonic $CO_2$ reduction using $H_2$ was performed in a flow reactor, and the catalyst bed thickness was kept at ∼1 mm, so that light photons penetrate each DPC-C4-Ni sphere across the catalyst bed (Scheme S1). Photocatalytic $CO_2$ reduction using different light intensities (without any external heating) as well as in the dark (with external heating) was carried out under a flow of $CO_2$ (10 mL/min) and $H_2$ (1 mL/min) and monitored using online micro gas chromatography (GC) (Figure 3a). We used a thin thermocouple and inserted it directly into the catalyst powder bed to measure its surface temperature, $T_s$ (Scheme S2). A high CO production rate of 2464 ± 40 mmol $g_{Ni}^{-1}$ $h^{-1}$ with 95% CO selectivity was achieved using DPC-C4-Ni at 2.7 W $cm^{-2}$ light intensity and $T_s$ reached 223 °C (no external heating). A small amount of $CH_4$ (5%) was also formed (Figure 3a,b). For control dark experiments, DPC-C4-Ni was evaluated at various temperatures (84, 136, 153, 183, 216, and 223 °C) using external heating, corresponding to different light intensities (Figure 3a). No product formation was observed up to 223 °C. At 300 °C, a CO production rate of only 272 mmol $g_{Ni}^{-1}$ $h^{-1}$ was observed as compared to 2464 mmol $g_{Ni}^{-1}$ $h^{-1}$ in the light (Figure 3a and Figure S15). Thus, DPC-C4-Ni showed 9 times more activity in light as compared to the dark.

To understand the intertwined thermal and nonthermal effects, we studied the catalyst response in successive light (L) and dark (D) modes. The product sampling time difference ($\Delta t$) was defined as the time between switching the light on or light off and the product quantification time (GC injection time). The catalyst became active as soon as we switched on the light (Figure 3c). However, $T_s$ took time to reach its maximum temperature. Also, on switching the light off, the production rate decreased sharply, whereas $T_s$ remained nearly the same (Figure S16a). If the thermal effect had been the only driving force in the catalysis reaction, the $CO_2$ production rate would not drop suddenly after the light was switched off, as $T_s$ was nearly the same for some time after the light was switched off (Figure S16a). The successive ten cycles of L and D showed the same fast response in every cycle (Figure S16b). The product selectivity of $CO_2$ hydrogenation also provided information about catalysis pathways. DPC-C4-Ni showed 95% CO selectivity and only 5% methane in light, whereas in the dark at 300 °C, it showed increased methane selectivity (20%). These experiments indicated that nonthermal effects played a pivotal role in $CO_2$ reduction. Several control experiments were also carried out using DPC-C4 and DFNS-Ni as catalysts under exactly the same photocatalytic conditions (Figure 3d). DPC-C4 showed no catalytic activity in light, even at 223 °C. DFNS-Ni showed no activity in light at 183 °C, while at 223 °C, a small amount of CO (2.1 mmol $g_{Ni}^{-1}$ $h^{-1}$) and methane (4.4 mmol $g_{Ni}^{-1}$ $h^{-1}$) was formed. This further indicated the role of plasmonic DPC-C4 in activating Ni sites. We also carried out $CO_2$ hydrogenation by DPC-C4-Ni without the $H_2$ reduction step to unravel the role of NiO in catalysis. However, in this case, no CO was formed, establishing $Ni^0$ as the active site and not NiO.

To confirm that $CO_2$ was the sole carbon source, a control experiment without $CO_2$ was carried out and neither CO nor $CH_4$ was detected (Figure 3d). An isotope experiment was conducted by replacing the normal $^{12}CO_2$ feed gas with isotopically labeled $^{13}CO_2$ gas, and the products were identified by GC-MS. The signal corresponds to $^{13}CO$ ($m/z$ = 29), and $^{13}CH_4$ ($m/z$ = 17) in the mass spectrum (Figure 3e,f), further confirming that the hydrogenated products originated from the $CO_2$ feed gas.

To understand the stability of DPC-C4-Ni, photocatalytic $CO_2$ hydrogenation was conducted for 100 h in a continuous-flow reactor (Figure 3g). Notably, the catalyst was stable for 100 h with a nearly constant CO production rate and CO selectivity. After catalysis, it showed no change in PXRD or light absorption behavior (Figures S17 and S18), while XPS showed a more metallic Ni phase due to *in situ* reduction


https://doi.org/10.1021/acsnano.2c10470
ACS Nano 2023, 17, 4526−4538

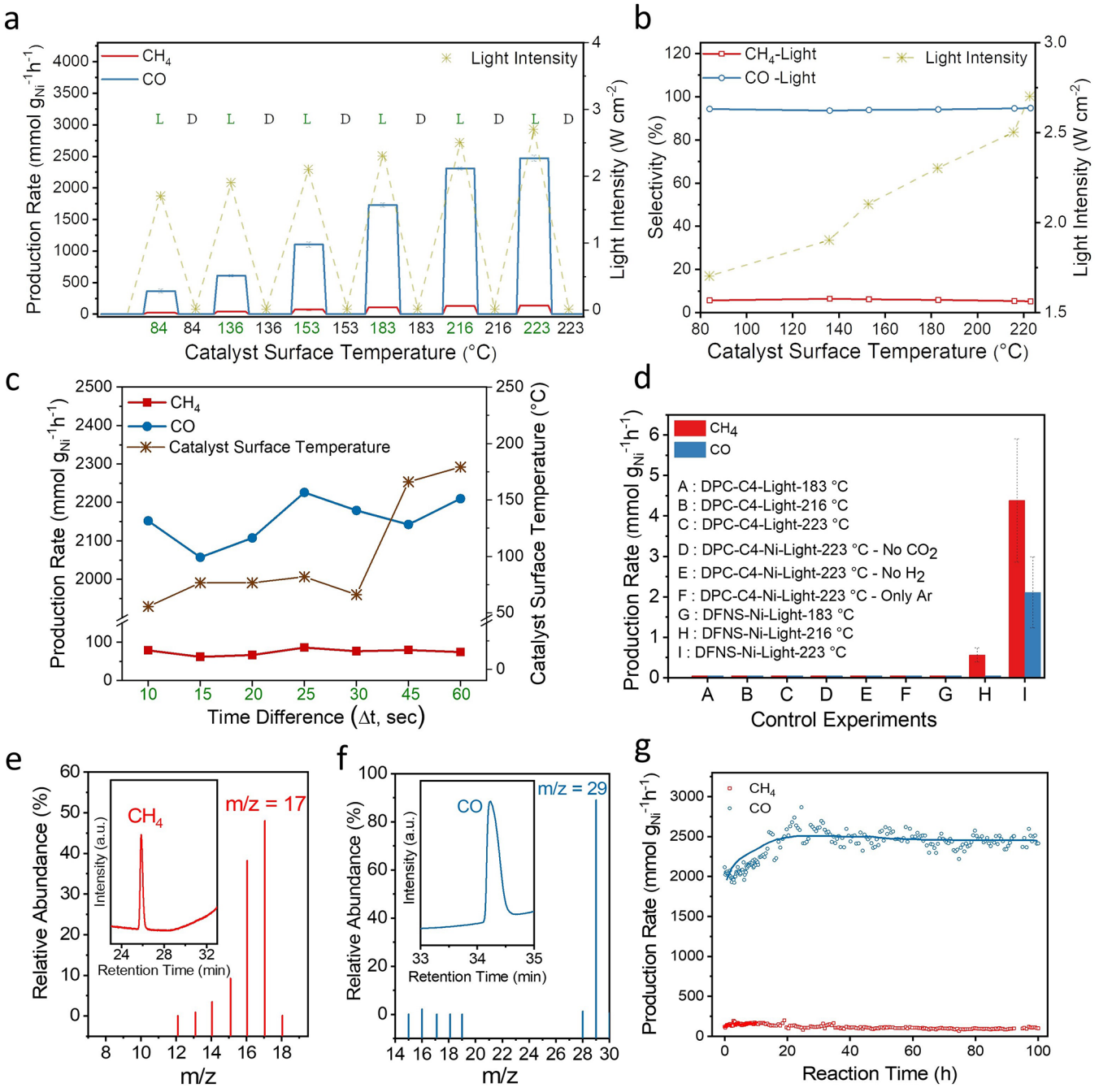


**Figure 3. Plasmonic $CO_2$ hydrogenation using DPC-C4-Ni. (a) Production rate and (b) selectivity of $CH_4$ and CO in light at various intensities and in dark at different temperatures: $H_2$ (1 mL $min^{-1}$), $CO_2$ (10 mL $min^{-1}$), 400−1100 nm using a xenon lamp. No external heating was used in the case of light experiments. (c) Production rate and catalyst surface temperature as a function of product sampling time difference ($\Delta t$). (d) Control experiments using different catalysts under various reaction conditions. Mass spectra of (e) $^{13}CH_4$ and (f) $^{13}CO$, obtained using labeled $^{13}CO_2$ as the feed. (g) Long-term stability study under the flow condition using light without external heating.**

during catalysis. TEM images and EDS elemental mapping of the spent catalyst indicate no sintering of nanoparticles (Figure S18), while a Raman analysis of the spent catalyst showed no carbon formation, indicating a coke-free $CO_2$ hydrogenation process due to the low temperature of the reaction (Figure S17d).

For a further understanding of the plasmonic activation mechanism, we studied the dependence of CO production rate on light intensity (Figure 4a). We monitored the surface temperature of the catalyst, which was found to be in the range of 84−223 °C (Scheme S2). We observed a linear dependence of CO production rate with light intensity (Figure 4a), indicating the presence of nonthermal pathways. In addition, the thermal effect was also playing its part, as, under light illumination, the population of excited vibrational states of adsorbed $CO_2$ and $H_2$ on DPC-C4-Ni increases, and these excited states need less energy to overcome the activation barrier, thus reducing the overall activation energy barrier of the reaction (Figure 4b,c).

Figure 4b shows the Arrhenius plot for the apparent activation energy barrier ($E_{app}$) of $CO_2$ hydrogenation to CO in light using DPC-C4-Ni and also in the dark at various


https://doi.org/10.1021/acsnano.2c10470
ACS Nano 2023, 17, 4526−4538

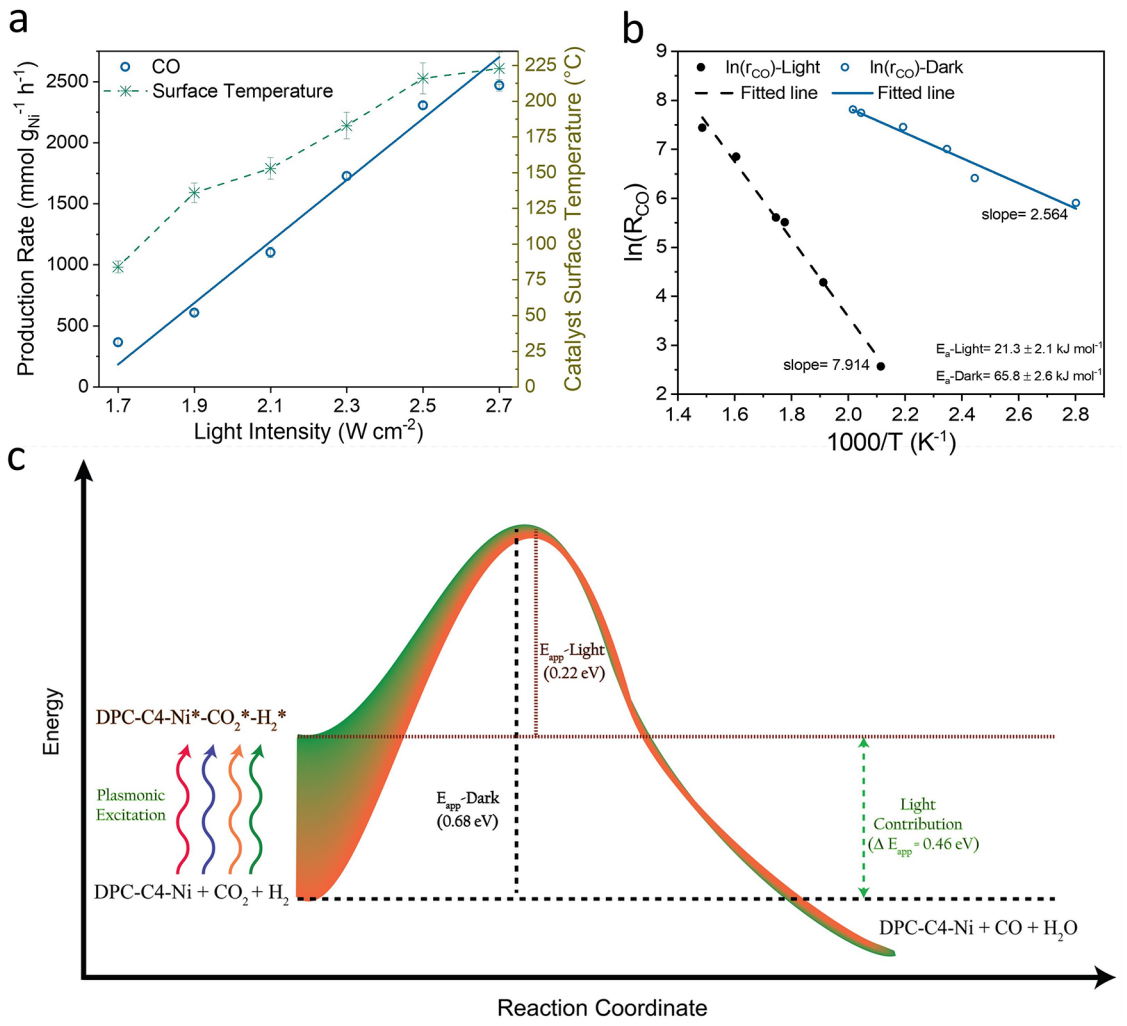


**Figure 4. (a) CO production rate (and respective catalyst surface temperature) plotted as a function of light intensity. (b) Arrhenius plot for $E_{app}$ of the $CO_2$ hydrogenation in the dark and in light. The slope of each curve gave the activation energy. (c) Plasmonic mechanism of lowering of the activation energy barrier.**

catalyst surface temperatures. The $E_{app}$ for the reaction in light was 21.3 ± 2.1 kJ $mol^{-1}$, whereas $E_{app}$ for the reaction in the dark was 65.8 ± 2.6 kJ $mol^{-1}$. This indicates a large decrease in the activation energy barrier, $\Delta E_{app} \approx 44.4$ kJ $mol^{-1}$, from dark to visible light due to plasmonic excitation (Figure 4c). Thus, because of the low activation barrier for $CO_2$ hydrogenation to CO in light, the reaction rate was extremely fast, as both the CO desorption and $\pi$-bond cleavage were accelerated by plasmonic excitation. The observed photoenhancement in the production rate of CO also indicated the role of the nonthermal pathway in the $CO_2$ hydrogenation, and the thermal effect played a minimal role in the $CO_2$ hydrogenation (Figure S19, Supplementary Note-2, and Excel sheet-2).[14,49] We then carried out light-wavelength-dependent catalysis (Figure S20). Since black gold is a broad-band light absorber, we did not observe wavelength-dependent activity in the visible range. Hence, it was difficult to differentiate various optical absorption channels. When we used pure IR light (808 nm), the catalytic activity was drastically reduced (Figure S20), indicating plasmonic excitation is only possible in the visible range and the photothermal channel was not efficient in DPC-C4-Ni.

We conducted the $CO_2$ hydrogenation reaction at various light intensities and temperatures (Figure 5). We observed the superlinear dependence of CO production on the light intensity with a power law exponent of 5.6 (rate $\propto I^n$) (Figure 5a). This behavior of plasmonic catalysts was reported to be a signature of multielectron-driven plasmonic reactions.[21]

It is known that plasmonic catalysts generally show a positive relationship between the reaction temperature and the reaction rate in light.[21] We also observed this positive relationship for DPC-C4-Ni; at a constant light intensity, the CO production rate increased with an increase in reaction temperature (Figure 5b,c). Notably, the quantum efficiency of this $CO_2$ hydrogenation process by black gold-Ni increased with an increase in reaction temperature at constant light intensity (Figure 5d). This is yet another confirmation of hot-carrier-assisted plasmonic photocatalysis.[21]

To further confirm the role of hot electrons, experiments were carried out to study the kinetic isotope effect (KIE) of photocatalytic $CO_2$ hydrogenation using $^{13}CO_2$ and $^{12}CO_2$ in light and dark (Figure 6a). We observed enhanced KIE in light (1.91) as compared to dark (~1), which again indicated the electron-driven plasmonic $CO_2$ hydrogenation. The difference in reaction rate for $^{13}CO_2$ vs $^{12}CO_2$ was due to different masses of these isotopes, with the lighter isotope $^{12}CO_2$ experiencing more acceleration (as compared to the heavier $^{13}CO_2$ isotope) under plasmonic excitation, reaching higher vibrational states


https://doi.org/10.1021/acsnano.2c10470
ACS Nano 2023, 17, 4526−4538

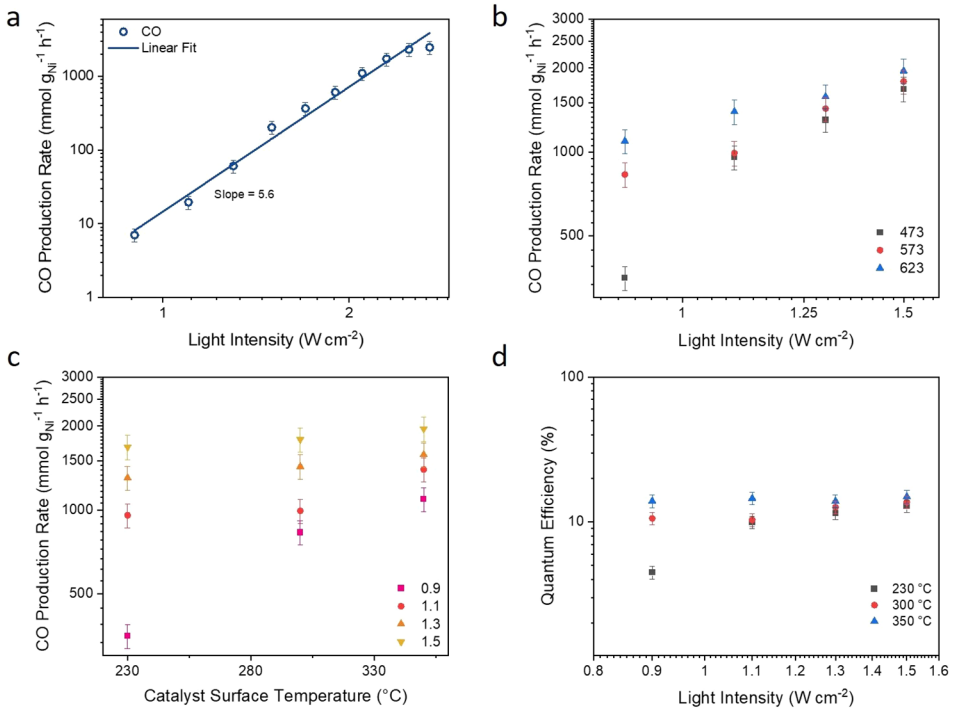


**Figure 5. Photocatalytic reaction rate and quantum efficiency as a function of light intensity and reaction temperature. (a) CO production rate (log scale) as a function of light intensity (log scale). The slope value gives the power law exponent number. (b) CO production rate (log scale), as a function of light intensity (log scale) at various temperatures. (c) CO photocatalytic rate (log scale) as a function of reaction temperature at various light intensities. (d) Quantum efficiency (%) (log scale) as a function of light intensity (log scale) at various reaction temperatures. For detailed calculations, refer to Supplementary Note-1 and Excel sheet-1 in the Supporting Information.**

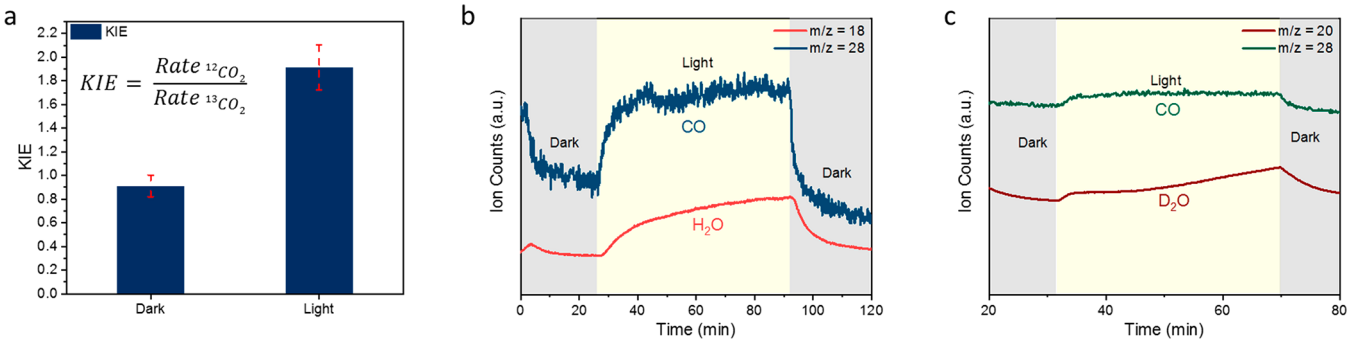


**Figure 6. (a) KIE for $CO_2$ hydrogenation, measured in dark and light. Ion signals of CO during the DPC-C4-Ni-catalyzed reactions of (b) $^{12}CO_2$ + $H_2$ and (c) $^{12}CO_2$ + $D_2$, in light.**

and, hence, more reaction probability.[21] In order to investigate the role of hydrogen gas, we conducted plasmonic $CO_2$ hydrogenation by replacing $H_2$ gas with $D_2$ and the signal corresponding to the formation of $D_2O$ was observed in a mass spectrometer (Figure 6b,c). This indicated that $H_2$ was acting as a hole quencher.

To get insight into the electron transfer rates, we studied the reduction of ferricyanide $[Fe(CN)_6]^{3-}$ to ferrocyanide $[Fe(CN)_6]^{4-}$, catalyzed by DPC-C4 and DPC-C4-Ni (Figure S21). The photocatalytic rate catalyzed by DPC-C4-Ni was 6.3 × $10^{-3}$ $min^{-1}$, 1.2 times more than that of DPC-C4 (5.6 × $10^{-3}$ $min^{-1}$). The higher rate of electron transfer in the case of DPC-C4-Ni than DPC-C4 suggests hot electron transfer from Au to Ni, which was then used to catalyze the reduction of $Fe^{3+}$ to $Fe^{2+}$. We then carried out $CO_2$ hydrogenation in the presence of an electron-accepting molecule, methyl-*p*-benzoquinone (MQ),[50,51] during $CO_2$ hydrogenation (experimental details in SI). We found that on adding MQ, the CO production rate drops drastically, from 2450 mmol $g_{Ni}^{-1}h^{-1}$ to 175 mmol $g_{Ni}^{-1}h^{-1}$ (Figure S22). This indicates that the MQ competed with $CO_2$ for hot electrons to reduce itself to methyl-*p*-hydroquinone, and this resulted in the drop in $CO_2$ reduction reaction and hence CO production rate.

***Operando* DRIFTS Studies for $CO_2$ Hydrogenation Mechanism.** *In situ* DRIFTS[12] spectra were acquired in the dark and in the light during the $CO_2$ reduction (Scheme S3 and Figure 7). DRIFT spectra in the light exhibited a strong peak centered at 2042 $cm^{-1}$ assigned to C═O (double bond between C and O) stretching vibrations of linearly bonded CO atop a Ni atom ($Ni^0$–CO)[12] (Figure 7d). A weak signal centered at 1931 $cm^{-1}$ was assigned to bridge carbonyl species, i.e., CO bonded to three neighboring Ni atoms of Ni NPs.[12] There was no signal at ~3015 $cm^{-1}$ (Figure 7b) or ~1591


https://doi.org/10.1021/acsnano.2c10470
ACS Nano 2023, 17, 4526−4538

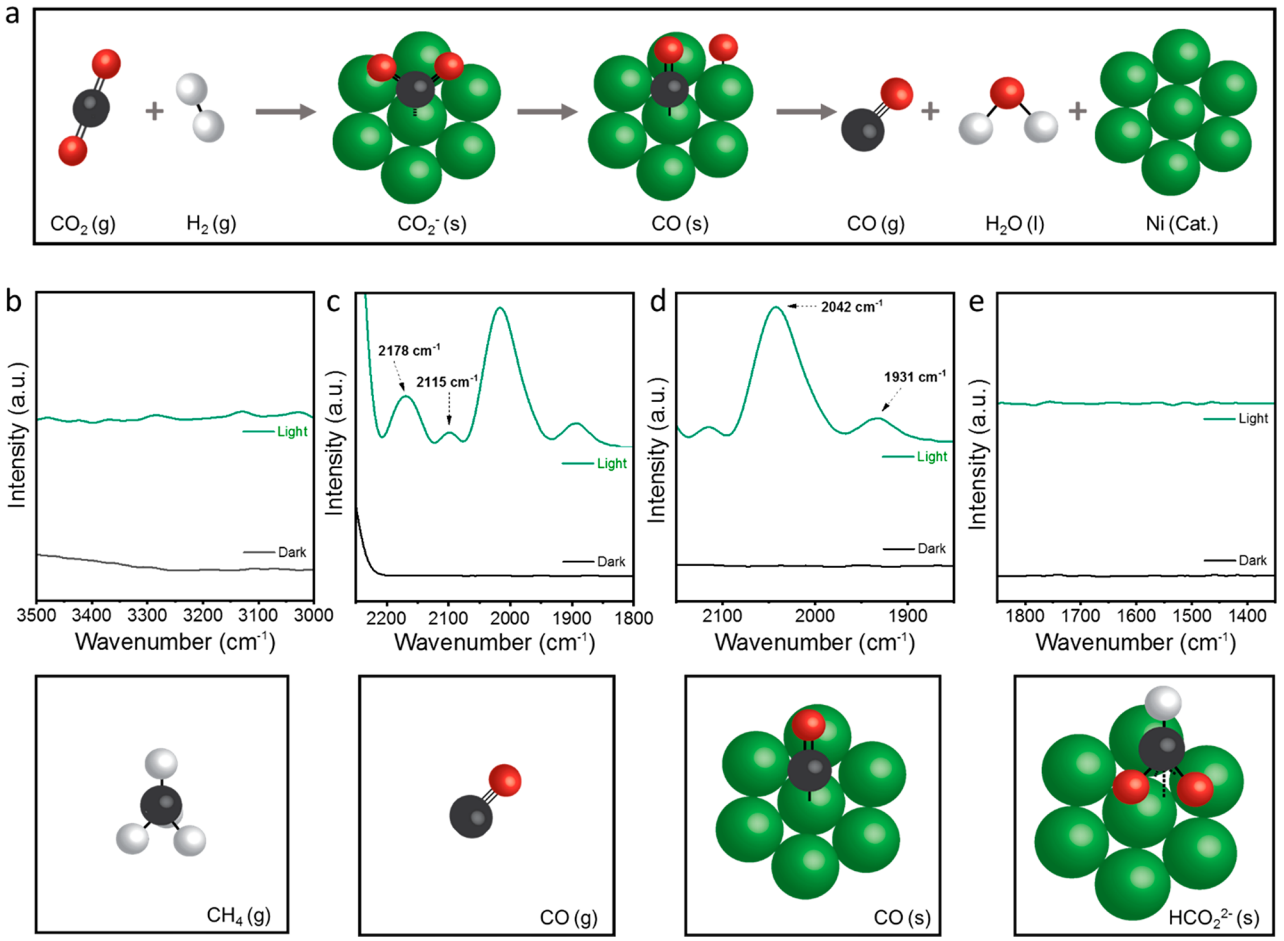


**Figure 7. (a) Schematic of $CO_2$ hydrogenation mechanism via direct dissociation. *In situ* DRIFT spectra with peaks for (b) methane, (c) gaseous CO, (d) adsorbed CO, and (e) adsorbed formate species in the light. For DRIFTS experiments in the light, no external heating was used.**

$cm^{-1}$ (Figure 7e), indicating the absence of gaseous methane and adsorbed formate species, respectively.[12]

This showed that $CO_2$ hydrogenation was taking place by a direct dissociation path (Figure 7a). The linearly bonded CO on Ni sites of DPC-C4-Ni were weakly bonded due to its weak Ni−C bond (as compared to trifold bridge bonded CO), and hence CO desorption was efficient, restricting further hydrogenation to methane and hence leading to more than 95% CO selectivity. DRIFT spectra showed intense peaks for gaseous CO and CO adsorbed on silica at 2178 and 2115 $cm^{-1}$ (Figure 7c), confirming the weak CO−Ni bonding and swift CO desorption.[12] After flushing, the peak for $CO_{ads}$ was absent in DRIFT spectra, further confirming the weak bonding of CO with Ni sites. These peaks were absent in the dark (Figure 7b−e, bottom spectra), due to no $CO_2$ hydrogenation under these conditions.

Due to highly dispersed Ni sites on DPC-C4, expedited formation of linearly bonded $Ni^0$−CO was favored, while strong multicoordinate Ni bonding to CO was disfavored (Figure 7). This allowed fast kinetics and high CO productivity, in addition to good selectivity. However, Weckhuysen et al.[12] observed that Ni nanoparticles below 2 nm, due to their lower d-band energy, caused slow desorption of CO and hence showed poor catalytic performance. In our catalytic system, even after the small size of Ni NPs, catalytic performance was good. This contradictory observation is explained using the concept of plasmonic excitation.[52−56] In the case of DPC-C4-Ni, the hypothesis was hot electrons are either generated in Ni due to an intense electric field within black gold hot spots (a direct mechanism) or charges are first generated in a black gold antenna and then injected into the Ni reactor (an indirect mechanism) (Figure 8a). A fraction of these hot electrons then interact with reactant $CO_2$, activating it and lowering the activation energy barrier. Also, during the damping of black gold LSPR, electrons in the nickel d-band can be excited to higher energy levels (hot electrons). Also, the filling of the Ni d-band due to hot-electron transfer from Au to Ni can take place. Ultrafast transient absorption spectroscopy (TAS) measurements were performed to study the involvement of hot electrons and their transfer to Ni (Figure 8).

The transient result (pumped−unpumped) reveals the characteristic negative signal (bleach) centered at the laser wavelength excitation and two positive signals or "winglets", as reported elsewhere.[57−59] The signal dynamics contains information about electron−electron (e-e), electron−phonon (e-ph), and phonon−phonon (ph-ph) scattering. The e-ph lifetime relates to Au NP electronic heat capacity, which is proportional to both the electronic temperature and the electron density, making it highly sensitive to the electronic structure of the metal.[60]

Figure 8b,c shows the contour plots of DPC-C4 and DPC-C4-Ni. Both maps are dominated by a Au plasmon signal with



https://doi.org/10.1021/acsnano.2c10470
ACS Nano 2023, 17, 4526−4538

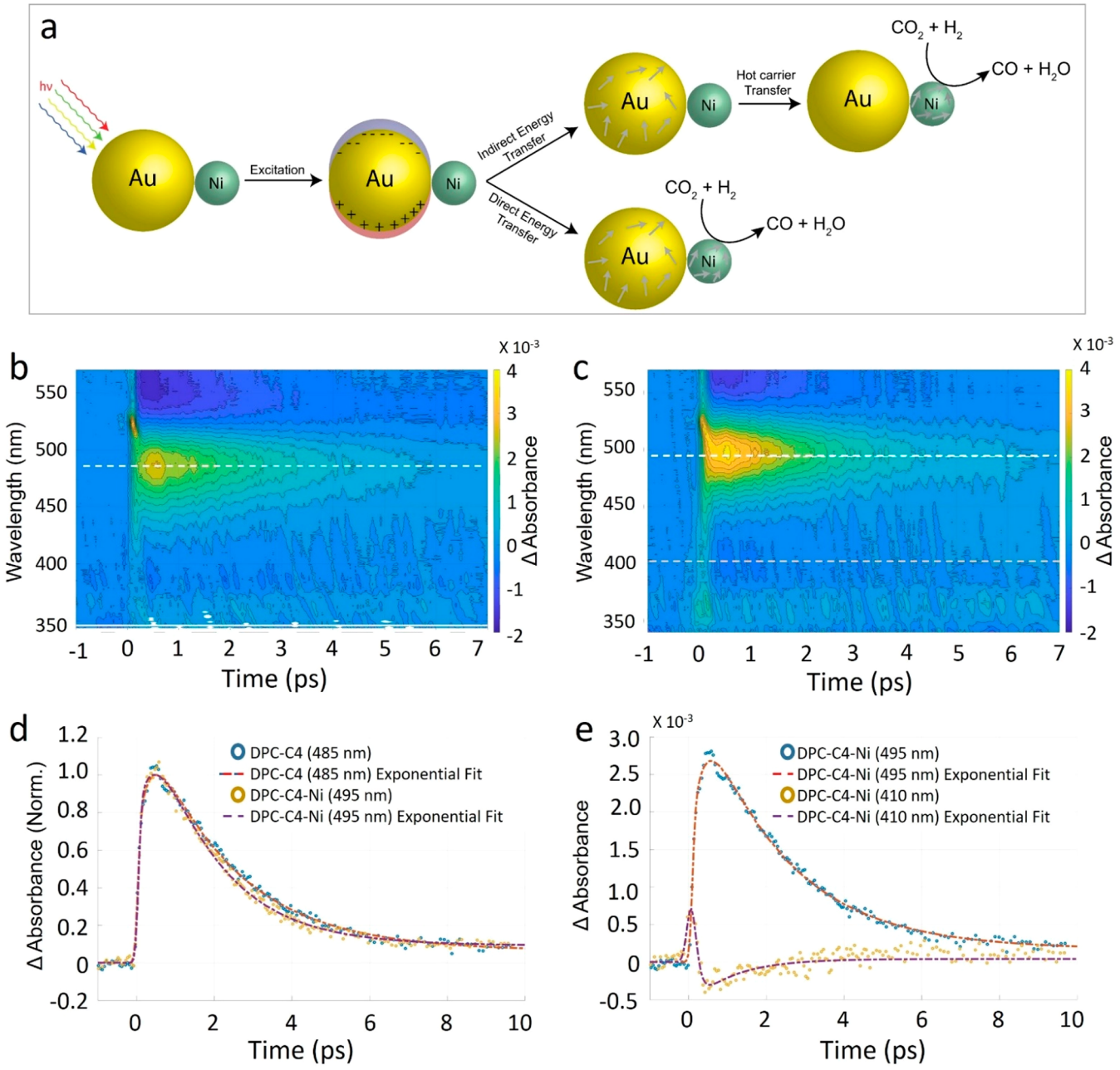


**Figure 8. (a) Schematic of direct vs indirect energy transfer processes that can result in hot-electron population in a Ni reactor. Surface plots of (b) DPC-C4 and (c) DPC-C4-Ni. (d) Kinetic trace extracted at the maximum of the winglet (white dotted lines on surface plots) for both samples and (e) kinetic trace extracted at the minimum of bleach observed at around 410 nm for DPC-C4-Ni (red dotted line on DPC-C4-Ni surface plot). The signal is overplotted with a kinetic trace for plasmon decay to compare kinetics. Experimental details are given in the Experimental Section in the Suppporting Information.**

characteristic positive winglet (450−520 nm) and bleach (520−600 nm). The winglets to the red of the bleach signal were omitted for visualization purposes. Kinetic traces extracted at the maximum of the winglets are presented in Figure 8d. The increasing component relates to the formation of hot carriers and elastic e-e scattering. We estimated the processes to be 302 ± 63 and 419 ± 107 fs for DPC-C4 and DPC-C4-Ni, respectively. The first decay provides information on the e-ph scattering lifetime. This was estimated using an exponential function to be 2.16 ± 0.11 and 1.64 ± 0.12 ps for DPC-C4 and DPC-C4-Ni, respectively. The reduction of e-ph lifetime observed in the DPC-C4-Ni sample compared to DPC-C4 relates to changes in the plasmon electronic structure consistent with hot carrier transfer from Au to Ni.[61,62] The final components were estimated to be 311.9 ± 79.3 and 429.5 ± 141 ps for DPC-C4 and DPC-C4-Ni, respectively, and relate to the ph-ph scattering events leading to heat release to the surroundings.

The observed changes in e-ph lifetime cannot be used to identify which kind of charge was transferred from Au to Ni. However, a careful analysis of the surface plots reveals a negative signal centered at 410 nm in the DPC-C4-Ni sample, which is absent in the DPC-C4 sample. The signal has an increasing component with a maximum at around 0.54 ps and a lifetime of 1.09 ± 0.69 ps, which mirrors the e-ph signal of the sample (Figure 8e). The signal appears in the region where


https://doi.org/10.1021/acsnano.2c10470
ACS Nano 2023, 17, 4526−4538

one may expect the Ni d−d transitions.[63,64] Moreover, the negative direction of the signal suggests a decrease in the empty states in the Ni d-band, which is consistent with hot-electron donation from Au to Ni. The existence of an increasing component of the signal with its maximum after the elastic e-e relaxation suggests that changes in Ni electron density occur after the formation of hot carriers. This allied to the observed changes in e-ph lifetime means that the hot electrons generated from the indirect process are transferred to Ni sites. The direct hot carrier generation in Ni due to the intense electric field of DPC-C4 can also take place; however, this should yield a nearly instantaneous change in Ni electron density, which is not consistent with our observations. Therefore, we propose the indirect hot-electron generation mechanism has the leading component for Ni electronic changes and, consequently, its catalytic behavior. However, the direct hot carrier generation in Ni due to the intense electric field of DPC-C4 should also be taking place, and the overall hot carrier population in DPC-C4-Ni was the combination of both direct and indirect hot-electron generation mechanisms.

**Comparison with Best Reported Photocatalytic Systems.** When DPC-C4-Ni was compared with some of the best-reported photocatalysts (plasmonic and semiconducting) for $CO_2$ to CO conversion,[65−83] we found that DPC-C4-Ni shows a high production rate and high stability (Figure S24 and Table S1). Our catalyst showed 2464 ± 40 mmol $g_{Ni}^{-1}$ $h^{-1}$ CO production, i.e., ∼182 times higher (in the flow) (Table S1), using only light without any external heating.

We have also compared DPC-C4-Ni with other reported $CO_2$ hydrogenation plasmonic catalysts,[17,84−87] where water in combination with sacrificial agents was used instead of hydrogen gas. The activity of all these catalysts was very low, with less than 100 $\mu$mol $g^{-1}$ $h^{-1}$ productivity of total products,[17,84−87] as compared to 2464 ± 40 mmol $g_{Ni}^{-1}$ $h^{-1}$ for DPC-C4-Ni. This indicates that generating hydrogen from water separately and then reacting the produced green hydrogen with $CO_2$ using a plasmonic photocatalyst is a more sustainable $CO_2$ hydrogenation path.

## CONCLUSIONS

We have demonstrated that plasmonic black gold-nickel efficiently catalyzes $CO_2$ hydrogenation using visible light. The reaction took place at temperatures as low as 84−223 °C without external heating. We found a multifold increase in the catalytic activity as compared to DPC-C4 to the extent that measurable photoactivity was only observed with DPC-C4-Ni. It showed the best-reported CO production rate of 2464 ± 40 mmol $g_{Ni}^{-1}$ $h^{-1}$ and a selectivity greater than 95% under the flow conditions. The catalyst showed extraordinary stability (100 h).

Superlinear power-law dependence on the light intensity (power law exponent of 5.6) with photocatalytic quantum efficiencies increased with an increase in light intensity and reaction temperature, while the kinetic isotope effect (KIE) in the light (1.91) was higher than that in the dark (∼1), confirming the hot-electron-mediated reaction mechanism. Ultrafast studies of hot-carrier dynamics proved the superfast electron injection from Au to Ni, populating the Ni reactor with charge carriers. We observed a spectral signature of such an indirect charge generation due to hot-electron transfer from the gold to the nickel. Finite-difference time-domain simulations also showed plasmon-induced high local field intensity enhancement in DPC-C4-Ni.

An *in situ* DRIFTS study showed C═O stretching vibrations of linearly bonded CO atop a Ni atom, while bridge carbonyl species formation was hindered. $CO_2$ hydrogenation took place by a direct dissociation path via linearly bonded nickel−CO. The linearly bonded CO on Ni sites of DPC-C4-Ni were weakly bonded due to its weak Ni−C bond. Hence CO desorption was efficient, restricting hydrogenation to methane, leading to more than 95% CO selectivity.

The high production rate and selectivity were due to Ni NPs being highly dispersed on black gold, providing a weakly bonded CO pathway, in addition to the excellent light-harvesting ability of black gold. Due to the excitation of electrons in the nickel d-band to a higher energy level during plasmonic damping of black gold SPR, as well as to filling of Ni d-band due to hot electron transfer from black gold to Ni, Ni sites showed excellent activity even at a smaller particle size. The excellent catalytic performance of black gold-Ni indicates the potential use of black gold to design innovative catalysts for a range of other reactions in addition to $CO_2$ reduction.

## METHODS

Experimental methods for the synthesis of dendritic plasmonic colloidosomes (black gold) as well as methods for plasmonic photocatalysis in the flow reactor for $CO_2$ hydrogenation, and $H_2$/$D_2$ dissociation are given in the Supporting Information.

## ASSOCIATED CONTENT

### Supporting Information

The Supporting Information is available free of charge at https://pubs.acs.org/doi/10.1021/acsnano.2c10470.

Experimental details for the synthesis of the catalyst, catalyst characterizations, CO-DRIFT study, finite-difference time-domain (FDTD) simulations, transient absorption spectroscopy (TAS) study, KIE, quantum efficiency, photoluminescence, plasmonic $CO_2$ reduction, and *operando* DRIFTS study (PDF)

Calculation of the quantum efficiency of the photocatalytic $CO_2$ hydrogenation process (XLSX)

Calculation of the thernal and nonthermal rates (XLSX)

## AUTHOR INFORMATION


### Corresponding Author

**Vivek Polshettiwar** − *Department of Chemical Sciences, Tata Institute of Fundamental Research (TIFR), Mumbai 400005, India*; orcid.org/0000-0003-1375-9668; Email: vivekpol@tifr.res.in

### Authors

**Rishi Verma** − *Department of Chemical Sciences, Tata Institute of Fundamental Research (TIFR), Mumbai 400005, India*

**Rajesh Belgamwar** − *Department of Chemical Sciences, Tata Institute of Fundamental Research (TIFR), Mumbai 400005, India*

**Pratip Chatterjee** − *Department of Chemical Sciences, Tata Institute of Fundamental Research (TIFR), Mumbai 400005, India*

**Robert Bericat-Vadell** − *Department of Chemistry-Ångström Laboratory, Uppsala University, Uppsala 75120, Sweden*

**Jacinto Sa** − *Department of Chemistry-Ångström Laboratory, Uppsala University, Uppsala 75120, Sweden*; orcid.org/0000-0003-2124-9510




https://doi.org/10.1021/acsnano.2c10470
*ACS Nano* 2023, 17, 4526−4538

Complete contact information is available at:
https://pubs.acs.org/10.1021/acsnano.2c10470

### Notes

The authors declare no competing financial interest.

## ACKNOWLEDGMENTS

We acknowledge the funding support of the Department of Atomic Energy (under project no. 12-R&D-TFR-RTI4003) and Mission Innovation India, Department of Science & Technology, Government of India. We acknowledge the XRD facility of TIFR, Mumbai, and EM facility of IIT, Mumbai, and Ms. Bhagyashree Chalke of TIFR, Mumbai. We thank Prof. Vaibhav Prabhudesai and Mr. Sukantu Das (Dept. of Nuclear and Atomic Physics) and Prof. Achanta Venugopal and Mr. Abhinav Kala (Dept. of Condensed Matter Physics & Materials Science) of TIFR, Mumbai, for mass spectrometry and FDTD support, respectively. We also thank Prof. Kuo-Wei Huang of KAUST for electron microscopy imaging. R.B.-V. and J.S. acknowledge a grant from the Knut and Alice Wallenberg Foundation (KAW 2019.0071).

## REFERENCES

(1) Gao, W.; Liang, S.; Wang, R.; Jiang, Q.; Zhang, Y.; Zheng, Q.; Xie, B.; Toe, C. T.; Zhu, X.; Wang, J.; Liang Huang, L.; Gao, Y.; Wang, Z.; Jo, C.; Wang, Q.; Wang, L.; Liu, Y.; Louis, B.; Scott, J.; Roger, A. C.; Amal, R.; Heh, H.; Park, S. E. Industrial Carbon Dioxide Capture and Utilization: State of the Art and Future Challenges. *Chem. Soc. Rev.* **2020**, *49*, 8584−8686.

(2) Ghoussoub, M.; Xia, M.; Duchesne, P. N.; Segal, D.; Ozin, G. A. Principles of Photothermal Gas-Phase Heterogeneous $CO_2$ Catalysis. *Energy Environ. Sci.* **2019**, *12*, 1122.

(3) Solomon, S.; Plattner, G.-K.; Knutti, R.; Friedlingstein, P. Irreversible Climate Change Due to Carbon Dioxide Emissions. *Proc. Natl. Acad. Sci. U. S. A.* **2009**, *106* (6), 1704−1709.

(4) Sun, S.; Sun, H.; Williams, P. T.; Wu, C. Recent Advances in Integrated $CO_2$ Capture and Utilization: A Review. *Sustain. Energy Fuels* **2021**, *5*, 4546−4559.

(5) Hepburn, C.; Adlen, E.; Beddington, J.; Carter, E. A.; Fuss, S.; Dowell, N. M.; Minx, J. C.; Smith, P.; Williams, C. K. The Technological and Economic Prospects for $CO_2$ Utilization and Removal. *Nature* **2019**, *575*, 87−97.

(6) Zhang, Z.; Mao, C.; Meira, D. M.; Duchesne, P. N.; Tountas, A. A.; Li, Z.; Qiu, C.; Tang, S.; Song, R.; Ding, X.; Sun, J.; Yu, J.; Howe, J. Y.; Tu, W.; Wang, L.; Ozin, G. A. New Black Indium Oxide—Tandem Photothermal $CO_2$-$H_2$ Methanol Selective Catalyst. *Nat. Commun.* **2022**, *13*, 1512.

(7) Zhou, J.; Li, J.; Kan, L.; Zhang, L.; Huang, Q.; Yan, Y.; Chen, Y.; Liu, J.; Li, S. L.; Lan, Y. Q. Linking Oxidative and Reductive Clusters to Prepare Crystalline Porous Catalysts for Photocatalytic $CO_2$ Reduction with $H_2O$. *Nat. Commun.* **2022**, *13*, 4681.

(8) Yin, G.; Nishikawa, M.; Nosaka, Y.; Srinivasan, N.; Atarashi, D.; Sakai, E.; Miyauchi, M. Photocatalytic Carbon Dioxide Reduction by Copper Oxide Nanocluster-Grafted Niobate Nanosheets. *ACS Nano* **2015**, *9* (2), 2111−2119.

(9) Li, Y.; Li, B.; Zhang, D.; Cheng, L.; Xiang, Q. Crystalline Carbon Nitride Supported Copper Single Atoms for Photocatalytic $CO_2$ Reduction with Nearly 100% CO Selectivity. *ACS Nano* **2020**, *14*, 10552−10561.

(10) Zhao, H.; Yu, R.; Ma, S.; Xu, K.; Chen, Y.; Jiang, K.; Fang, Y.; Zhu, C.; Liu, X.; Tang, Y.; Wu, L.; Wu, Y.; Jiang, Q.; He, P.; Liu, Z.; Tan, L. The Role of $Cu_1$−$O_3$ Species in Single-Atom $Cu/ZrO_2$ Catalyst for $CO_2$ Hydrogenation. *Nat. Catal* **2022**, *5*, 818−831.

(11) Ulmer, U.; Dingle, T.; Duchesne, P. N.; Morris, R. H.; Tavasoli, A.; Wood, T.; Ozin, G. A. Fundamentals and Applications of Photocatalytic $CO_2$ Methanation. *Nat. Commun.* **2019**, *10*, 3169.

(12) Vogt, C.; Groeneveld, E.; Kamsma, G.; Nachtegaal, M.; Lu, L.; Kiely, C. J.; Berben, P. H.; Weckhuysen. B. M. Unravelling Structure Sensitivity in $CO_2$ Hydrogenation Over Nickel. *Nat. Catal.* **2018**, *1*, 127−134.

(13) Cai, M.; Wu, Z.; Li, Z.; Wang, L.; Sun, W.; Tountas, A. A.; Li, C.; Wang, S.; Feng, K.; Xu, A. B.; Tang, S.; Tavasoli, A.; Peng, M.; Liu, W.; Helmey, A. S.; He, L.; Ozin, G. A.; Zhang, X. Greenhouse-Inspired Supra-Photothermal $CO_2$ Catalysis. Nat. *Energy* **2021**, *6*, 807−814.

(14) Camargo, C. H. P.; Cortés, E. *Plasmonic Catalysis: From Fundamentals to Applications*; Wiley-VCH: 2021.

(15) Aslam, U.; Rao, V. G.; Chavez, S.; Linic, S. Catalytic Conversion of Solar to Chemical Energy on Plasmonic Metal Nanostructures. *Nat. Catal.* **2018**, *1*, 656−665.

(16) Cortés, E.; Besteiro, L. V.; Alabastri, A.; Baldi, A.; Tagliabue, G.; Demetriadou, A.; Narang, P. Challenges in Plasmonic Catalysis. *ACS Nano* **2020**, *14*, 16202−16219.

(17) Yu, S.; Jain, P. K. Plasmonic Photosynthesis of C1−C3 Hydrocarbons from Carbon Dioxide Assisted by an Ionic Liquid. *Nat. Commun.* **2019**, *10*, 2022.

(18) Lian, Z.; Sakamoto, M.; Matsunaga, H.; Vequizo, J. J. M.; Yamakata, A.; Haruta, M.; Kurata, H.; Ota, W.; Sato, T.; Teranishi, T. Near Infrared Light Induced Plasmonic Hot Hole Transfer at a Nano-Heterointerface. *Nat. Commun.* **2018**, *9*, 2314.

(19) Kamarudheen, R.; Aalbers, G. J. W.; Hamans, R. F.; Kamp, L. P. J.; Baldi, A. Distinguishing Among All Possible Activation Mechanisms of a Plasmon-Driven Chemical Reaction. *ACS Energy Lett.* **2020**, *5*, 2605−2613.

(20) Mittal, D.; Ahlawat, M.; Rao, V. G. Recent Progress and Challenges in Plasmon-Mediated Reduction of $CO_2$ to Chemicals and Fuels. *Adv. Mater. Interfaces* **2022**, *9*, 2102383.

(21) Christopher, P.; Xin, H.; Marimuthu, A.; Linic, S. Singular Characteristics and Unique Chemical Bond Activation Mechanisms of Photocatalytic Reactions on Plasmonic Nanostructures. *Nat. Mater.* **2012**, *11*, 1044−1050.

(22) An, X.; Kays, J. C.; Lightcap, I. V.; Ouyang, T.; Dennis, A. M.; Reinhard, B. M. Wavelength-Dependent Bifunctional Plasmonic Photocatalysis in Au/Chalcopyrite Hybrid Nanostructures. *ACS Nano* **2022**, *16*, 6813−6824.

(23) Plunkett, A.; Kampferbeck, M.; Bor, B.; Sazama, U.; Krekeler, T.; Bekaert, L.; Noei, H.; Giuntini, D.; Froba, M.; Stierle, A.; Weller, H.; Vossmeyer, T.; Schneider, G. A.; Domenech, B. Strengthening Engineered Nanocrystal Three-Dimensional Superlattices via Ligand Conformation and Reactivity. *ACS Nano* **2022**, *16*, 11692.

(24) da Silva, A. G. M.; Rodrigues, T. S.; Correia, V. G.; Alves, T. V.; Alves, R. S.; Ando, R. A.; Ornellas, F. R.; Wang, J. L.; Andrade, L. H.; Camargo, P. H. C. Plasmonic Nanorattles as Next-Generation Catalysts For Surface Plasmon Resonance-Mediated Oxidations Promoted by Activated Oxygen. *Angew. Chem., Int. Ed.* **2016**, *55*, 7111−7115.

(25) Tiburski, C.; Boje, A.; Nilsson, S.; Say, Z.; Fritzsche, J.; Ström, H.; Hellman, A.; Langhammer, C. Light-Off in Plasmon-Mediated Photocatalysis. *ACS Nano* **2021**, *15*, 11535−11542.

(26) Li, S.; Huang, H.; Shao, L.; Wang, J. How to Utilize Excited Plasmon Energy Efficiently. *ACS Nano* **2021**, *15* (7), 10759−10768.

(27) Koya, A. N.; Zhu, X.; Ohannesian, N.; Yanik, A. A.; Alabastri, A.; Zaccaria, R. P.; Krahne, R.; Shih, W. C.; Garoli, D. Nanoporous Metals: From Plasmonic Properties to Applications in Enhanced Spectroscopy and Photocatalysis. *ACS Nano* **2021**, *15* (4), 6038−6060.

(28) Collins, S. S. E.; Searles, E. K.; Tauzin, L. J.; Lou, M.; Bursi, L.; Liu, Y.; Song, J.; Flatebo, C.; Baiyasi, R.; Cai, Y. Y.; Foerster, B.; Lian, T.; Nordlander, P.; Link, S.; Landes, C. F. Plasmon Energy Transfer in Hybrid Nanoantennas. *ACS Nano* **2021**, *15* (6), 9522−9530.

(29) Pedrazo-Tardajos, A.; Arslan Irmak, E.; Kumar, V.; Sanchez-Iglesias, A.; Chen, Q.; Wirix, M.; Freitag, B.; Albrecht, W.; Van Aert, S.; Liz-Marzan, L. M.; Bals, S. Thermal Activation of Gold Atom Diffusion in Au@Pt Nanorods. *ACS Nano* **2022**, *16* (6), 9608−9619.

(30) Swearer, F. D.; Zhao, H.; Zhou, L.; Zhang, C.; Robatjazi, H.; Martirez, P. M. J.; Krauter, M. C.; Yazdi, S.; McClain, J. M.; Ringe, E.; Carter, A. E.; Nordlander, P.; Halas, N. J. Heterometallic Antenna−Reactor Complexes for Photocatalysis. *Proc. Natl. Acad. Sci. U. S. A.* **2016**, *113*, 8916−8920.
(31) Aslam, U.; Chavez, S.; Linic, S. Controlling Energy Flow in Multimetallic Nanostructures for Plasmonic Catalysis. *Nat. Nanotechnol.* **2017**, *12*, 1000−1005.
(32) Swearer, D. F.; Robatjazi, H.; Martirez, J. M. P.; Zhang, M.; Zhou, L.; Carter, E. A.; Nordlander, P.; Halas, N. J. Plasmonic Photocatalysis of Nitrous Oxide into $N_2$ and $O_2$ Using Aluminum-Iridium Antenna-Reactor Nanoparticles. *ACS Nano* **2019**, *13*, 8076−8086.
(33) Zhou, L.; Martirez, J. M. P.; Finzel, J.; Zhang, C.; Swearer, D. F.; Tian, S.; Robatjazi, H.; Lou, M.; Dong, L.; Henderson, L.; Christopher, P.; Carter, E. A.; Nordlander, P.; Halas, N. J. Light-Driven Methane Dry Reforming with Single Atomic Site Antenna-Reactor Plasmonic Photocatalysts. *Nat. Energy* **2020**, *5*, 61−70.
(34) Dongare, P. D.; Zhao, Y.; Renard, D.; Yang, J.; Neumann, O.; Metz, J.; Yuan, L.; Alabastri, A.; Nordlander, P.; Halas, N. J. A 3D Plasmonic Antenna-Reactor for Nanoscale Thermal Hotspots and Gradients. *ACS Nano* **2021**, *15*, 8761−8769.
(35) Robatjazi, H.; Bao, J. L.; Zhang, M.; Zhou, L.; Christopher, P.; Carter, E. A.; Nordlander, P.; Halas, N. J. Plasmon-Driven Carbon−Fluorine ($C(sp^3)$−F) Bond Activation with Mechanistic Insights into Hot-Carrier-Mediated Pathways. *Nat. Catal.* **2020**, *3*, 564−573.
(36) Dhiman, M.; Maity, A.; Das, A.; Belgamwar, R.; Chalke, B.; Lee, Y.; Sim, K.; Nam, J.-M.; Polshettiwar, V. Plasmonic Colloidosomes of Black Gold for Solar Energy Harvesting and Hotspots Directed Catalysis for $CO_2$ to Fuel Conversion. *Chem. Sci.* **2019**, *10*, 6594−6603.
(37) Maity, A.; Belgamwar, R.; Polshettiwar, V. . Facile Synthesis to Tune Size, Textural Properties and Fiber Density of Dendritic Fibrous Nanosilica for Applications in Catalysis and $CO_2$ Capture. *Nat. Protoc.* **2019**, *14*, 2177−2204.
(38) Mishra, A. K.; Belgamwar, R.; Jana, R.; Datta, A.; Polshettiwar, V. Defects in Nanosilica Catalytically Convert $CO_2$ to Methane without any Metal and Ligand. *Proc. Natl. Acad. Sci. U. S. A.* **2020**, *117*, 6383−6390.
(39) Maity, A.; Chaudhari, S.; Titman, J. J.; Polshettiwar, V. Catalytic Nanosponges of Acidic Aluminosilicates for Plastic Degradation and $CO_2$ to Fuel Conversion. *Nat. Commun.* **2020**, *11*, 3828.
(40) Polshettiwar, V. Dendritic Fibrous Nanosilica: Discovery, Synthesis, Formation Mechanism, Catalysis, and $CO_2$ Capture-Conversion. *Acc. Chem. Res.* **2022**, *55*, 1395−1410.
(41) Kyriakou, G.; Maárquez, A. M.; Holgado, J. P.; Taylor, M. J.; Wheatley, A. E. H.; Mehta, J. P.; Sanz, J. F.; Beaumont, S. K.; Lambert, R. M. Comprehensive Experimental and Theoretical Study of the CO + NO Reaction Catalyzed by Au/Ni Nanoparticles. *ACS Catal.* **2019**, *9*, 4919−4929.
(42) Leon, C. C.; Liu, Q.; Ceyer, S. T. CO Adsorption on Gold Nickel Au−Ni(111) Surface Alloys. *J. Phys. Chem. C* **2019**, *123*, 9041−9058.
(43) Yim, W.-L.; Nowitzki, T.; Necke, M.; Schnars, H.; Nickut, P.; Biener, J.; Biener, M. M.; Zielasek, V.; Al-Shamery, K.; Kluäner, T.; Baäumer, M. Universal Phenomena of CO Adsorption on Gold Surfaces with Low-Coordinated Sites. *J. Phys. Chem. C* **2007**, *111*, 445−451.
(44) Hadjiivanov, K.; Mihaylov, M.; Abadjieva, N.; Klissurski, D. Characterization of $Ni/TiO_2$ Catalysts Prepared by Successive Adsorption−Reduction of $Ni^{2+}$ Ions. *J. Chem. Soc. Farday Trans.* **1998**, *94*, 3711−3716.
(45) Li, J.-F; Li, C.-Y; Aroca, R. F. Plasmon-Enhanced Fluorescence Spectroscopy. *Chem. Soc. Rev.* **2017**, *46*, 3962.
(46) Mukherjee, S.; Libisch, F.; Large, N.; Neumann, O.; Brown, V. L.; Cheng, J.; Lassiter, L. J.; Carter, A. E.; Nordlander, P.; Halas, N. J. Hot Electrons Do the Impossible: Plasmon-Induced Dissociation of $H_2$ on Au. *Nano Lett.* **2013**, *13*, 240−247.
(47) He, S.; Huang, J.; Goodsell, J. L.; Angerhofer, A.; Wei, W. D. Plasmonic Nickel-$TiO_2$ Heterostructures for Visible-Light-Driven Photochemical Reactions. *Angew. Chem., Int. Ed.* **2019**, *58*, 6038−6041.
(48) Han, P.; Tana Tana, T.; Xiao, Q.; Sarina, S.; Waclawik, E. R.; Gomez, D. E.; Zhu, H. Promoting Ni(II) Catalysis with Plasmonic Antennas. *Chem.* **2019**, *5*, 2879−2899.
(49) Zhang, X.; Li, X.; Reish, M. E.; Zhang, D.; Su, N. Q.; utieárrez, Y.; Moreno, F.; Yang, W.; Everitt, H. O.; Liu, J. Plasmon-Enhanced Catalysis: Distinguishing Thermal and Nonthermal Effects. *Nano Lett.* **2018**, *18*, 1714−1723.
(50) Scott, D. T.; Mcknight, D. M.; Harris, E. B.; Kolesar, S. E.; Lovley, D. R. Quinone Moieties Act as Electron Acceptors in the Reduction of Humic Substances by Humics-Reducing Microorganisms. *Environ. Sci. Technol.* **1998**, *32*, 2984−2989.
(51) Huynh, M. T.; Anson, C. W.; Cavell, A. C.; Stahl, S. S.; Hammes-Schiffer, S. Quinone 1e- and 2 e-/2 H+ Reduction Potentials: Identification and Analysis of Deviations from Systematic Scaling Relationships. *J. Am. Chem. Soc.* **2016**, *138*, 15903−15910.
(52) Linic, S.; Chavez, S.; Elias, R. Flow and Extraction of Energy and Charge Carriers in Hybrid Plasmonic Nanostructures. *Nat. Mater.* **2021**, *20*, 916−924.
(53) Kumar, P. V.; Rossi, T. P.; Kuisma, M.; Erhart, P.; Norris, D. J. Direct Hot-Carrier Transfer in Plasmonic Catalysis. *Faraday Discuss.* **2019**, *214*, 189−197.
(54) Zhou, L.; Swearer, D. F.; Zhang, C.; Robatjazi, H.; Zhao, H.; Henderson, L.; Dong, L.; Christopher, P.; Carter, E. A.; Nordlander, P.; Halas, N. J. Quantifying Hot Carrier and Thermal Contributions in Plasmonic Photocatalysis. *Science* **2018**, *362*, 69−72.
(55) Dubi, Y.; Un, W. I.; Sivan, Y. Thermal Effects − An Alternative Mechanism for Plasmon-Assisted Photocatalysis. *Chem. Sci.* **2020**, *11*, 5017−5027.
(56) Kim, Y.; Smith, J. G.; Jain, P. K. Harvesting Multiple Electron−Hole Pairs Generated Through Plasmonic Excitation of Au Nanoparticles. *Nat. Chem.* **2018**, *10*, 763−769.
(57) Hodak, J. H.; Martini, I.; Hartland, G. V. Spectroscopy and Dynamics of Nanometer-Sized Noble Metal Particles. *J. Phys. Chem. B* **1998**, *102*, 6958−6967.
(58) Link, S.; El-Sayed, M. A. Optical Properties and Ultrafast Dynamics of Metallic Nanoparticles. *Annu. Rev. Phys. Chem.* **2003**, *54*, 331−366.
(59) Hartland, G. V. Optical Studies of Dynamics in Noble Metal Nanostructures. *Chem. Rev.* **2011**, *111*, 3858−3887.
(60) Brown, A. M.; Sundararaman, R.; Narang, P.; Goddard, W. A.; Atwater, H. A. Ab Initio Phonon Coupling and Optical Response of Hot Electrons in Plasmonic. *Phys. Rev. B* **2016**, *94*, 075120.
(61) Tagliabue, G.; DuChene, J. S.; Abdellah, M.; et al. Ultrafast Hot-Hole Injection Modifies Hot-Electron Dynamics in Au/P-GaN Heterostructures. *Nat. Mater.* **2020**, *19*, 1312−1318.
(62) Hattori, Y.; Meng, J.; Zheng, K.; Meier de Andrade, A.; Kullgren, J.; Broqvist, P.; Nordlander, P.; Sa, J. Phonon-Assisted Hot Carrier Generation in Plasmonic Semiconductor Systems. *Nano Lett.* **2021**, *21*, 1083−1089.
(63) Guo, H.; Chen, Y.; Chen, X.; Wen, R.; Yue, G.-H.; Peng, D.-L. Ultrafast Hot-Hole Injection Modifies Hot-Electron Dynamics in Au/P-GaN Heterostructures. *Nanotechnology* **2011**, *22*, 195604.
(64) Meftah, A. M.; Gharibshahi, E.; Soltani, N.; Yunus, W. M. M.; Saion, E. Structural, Optical and Electrical Properties of PVA/PANI/Nickel Nanocomposites Synthesized by Gamma Radiolytic Method. *Polymers* **2014**, *6*, 2435−2450.
(65) Xu, Y.-F.; Duchesne, P. N.; Wang, L.; Tavasoli, A.; Jelle, A. A.; Xia, M.; Liao, J.-F.; Kuang, D.-B.; Ozin, G. A. High-Performance Light-Driven Heterogeneous $CO_2$ Catalysis with Near-Unity Selectivity on Metal Phosphides. *Nat. Commun.* **2020**, *11*, 5149.
(66) Wu, Z.; Li, C.; Li, Z.; Feng, K.; Cai, M.; Zhang, D.; Wang, S.; Chu, M.; Zhang, C.; Shen, J.; Huang, Z.; Xiao, Y.; Ozin, G. A.; Zhang, X.; He, L. Niobium and Titanium Carbides (MXenes) as Superior Photothermal Supports for $CO_2$ Photocatalysis. *ACS Nano* **2021**, *15*, 5696−5705.


https://doi.org/10.1021/acsnano.2c10470
*ACS Nano* 2023, 17, 4526−4538

(67) Wang, L.; Dong, Y.; Yan, T.; Hu, Z. A.; Jelle, A. A.; Meira, D. M.; Duchesne, P. N.; Loh, J. Y. Y.; Qiu, C.; Storey, E. E.; Xu, Y.; Sun, W.; Ghoussoub, M.; Kherani, N. P.; Helmy, A. S.; Ozin, G. A. Black Indium Oxide a Photothermal $CO_2$ Hydrogenation Catalyst. *Nat. Commun.* **2020**, *11*, 2432.
(68) Martinez Molina, P.; Meulendijks, N.; Xu, M.; Verheijen, M. A.; Hartog, T.; Buskens, P.; Sastre, F. Low Temperature Sunlight-Powered Reduction of $CO_2$ to CO Using a Plasmonic Au/$TiO_2$ Nanocatalyst. *ChemCatChem.* **2021**, *13*, 4507−4513.
(69) Upadhye, A. A.; Ro, I.; Zenga, X.; Kim, H. J.; Tejedor, I.; Anderson, M. A.; Dumesic, J. A.; Hub, G. W. Plasmon-Enhanced Reverse Water Gas Shift Reaction Over Oxide Supported Au Catalysts. *Catal. Sci. Technol.* **2015**, *5*, 2590−2601.
(70) Wan, L.; Zhou, Q.; Wang, X.; Wood, T. E.; Wang, L.; Duchesne, P. N.; Guo, J.; Yan, X.; Xia, M.; Li, Y. F.; Jelle, A. A.; Ulmer, U.; Jia, J.; Li, T.; Sun, W.; Ozin, G. A. $Cu_2O$ Nanocubes with Mixed Oxidation-State Facets for (Photo)Catalytic Hydrogenation of Carbon Dioxide. *Nat. Catal.* **2019**, *2*, 889−898.
(71) Zhang, H.; Wang, T.; Wang, J.; Liu, H.; Dao, T. D.; Li, M.; Liu, G.; Meng, X.; Chang, K.; Shi, L.; Nagao, T.; Ye, J. Surface-Plasmon-Enhanced Photodriven $CO_2$ Reduction Catalyzed by Metal-Organic-Framework-Derived Iron Nanoparticles Encapsulated by Ultrathin Carbon Layers. *Adv. Mater.* **2016**, *28*, 3703−3710.
(72) Jia, Z.; Ning, S.; Tong, Y.; Chen, X.; Hu, H.; Liu, L.; Ye, J.; Wang, D. Selective Photothermal Reduction of $CO_2$ to CO over Ni-Nanoparticle/N-Doped $CeO_2$ Nanocomposite Catalysts. *ACS Appl. Nano Mater.* **2021**, *4*, 10485−10494.
(73) Zhao, J.; Yang, Q.; Shi, R.; Waterhouse, G. I. N.; Zhang, X.; Wu, L.-Z.; Tung, C.-H.; Zhang, T. FeO−$CeO_2$ Nanocomposites: An Efficient and Highly Selective Catalyst System for Photothermal $CO_2$ Reduction to CO. *NPG Asia Mater.* **2020**, *12*, 5.
(74) Fu, G.; Jiang, M.; Liu, J.; Zhang, K.; Hu, Y.; Xiong, Y.; Tao, A.; Tie, Z.; Jin, Z. Rh/Al Nanoantenna Photothermal Catalyst for Wide-Spectrum Solar-Driven $CO_2$ Methanation with Nearly 100% Selectivity. *Nano Lett.* **2021**, *21*, 8824−8830.
(75) Tahir, B.; Tahir, M.; Amin, N. A. S. Photocatalytic $CO_2$ Conversion over Au/$TiO_2$ Nanostructures for Dynamic Production of Clean Fuels in a Monolith Photoreactor. *Clean Techn. Environ. Policy* **2016**, *18*, 2147.
(76) Tahir, M.; Tahir, B.; Amin, N. A. S. Synergistic Effect in Plasmonic Au/Ag Alloy NPs Co-Coated $TiO_2$ NWs Toward Visible-Light Enhanced $CO_2$ Photoreduction to Fuels. *Appl. Catal. B: Environ.* **2017**, *204*, 548−560.
(77) Jia, J.; Wang, H.; Lu, Z.; O'Brien, P. G.; Ghoussoub, M.; Duchesne, P.; Zheng, Z.; Li, P.; Qiao, Q.; Wang, L.; Gu, A.; Jelle, A. A.; Dong, Y.; Wang, Q.; Ghuman, K. K.; Wood, T.; Qian, C.; Shao, Y.; Qiu, C.; Ye, M.; Zhu, Y.; Lu, Z.-H.; Zhang, P.; Helmy, A. S.; Singh, C. V.; Kherani, N. P.; Perovic, D. D.; Ozin, G. A. Photothermal Catalyst Engineering: Hydrogenation of Gaseous $CO_2$ with High Activity and Tailored Selectivity. *Adv. Sci.* **2017**, *4*, 1700252.
(78) Zhang, X.; Li, X.; Zhang, D.; Su, Q. N.; Yang, W.; Everitt, O. H.; Liu, J. Product Selectivity in Plasmonic Photocatalysis for Carbon Dioxide Hydrogenation. *Nat. Commun.* **2017**, *8*, 14542.
(79) Tahir, M.; Tahir, B.; Amin, N. A. S.; Zakaria, Z. Y. Photo-Induced Reduction of $CO_2$ to CO with Hydrogen over Plasmonic Ag-NPs/$TiO_2$ NWs Core/Shell Hetero-Junction under UV and Visible Light. *J. $CO_2$ Util.* **2017**, *18*, 250−260.
(80) Robatjazi, H.; Zhao, H.; Swearer, D. F.; Hogan, N. J.; Zhou, L.; Alabastri, A.; McClain, M. J.; Nordlander, P.; Halas, N. J. Plasmon-Induced Selective Carbon Dioxide Conversion on Earth-Abundant Aluminum-Cuprous Oxide Antenna-Reactor Nanoparticles. *Nat. Commun.* **2017**, *8*, 27.
(81) Sastre, F.; Puga, A. V.; Liu, L.; Corma, A.; García, H. Complete Photocatalytic Reduction of $CO_2$ to Methane by $H_2$ under Solar Light Irradiation. *J. Am. Chem. Soc.* **2014**, *136*, 6798−6801.
(82) Loh, J. Y. Y.; Mohan, A.; Flood, A. G.; Ozin, G. A.; Kherani, N. P. Waveguide Photoreactor Enhances Solar Fuels Photon Utilization Towards Maximal Optoelectronic − Photocatalytic Synergy. *Nat. Commun.* **2021**, *12*, 402.
(83) Stanley, J. N.G.; Garcia-Garcia, I.; Perfrement, T.; Lovell, E. C.; Schmidt, T. W.; Scott, J.; Amal, R. Plasmonic Effects on $CO_2$ Reduction over Bimetallic Ni-Au Catalysts. *Chem. Eng. Sci.* **2019**, *194*, 94−104.
(84) Yu, S.; Wilson, J. A.; Heo, J.; Jain, K. P. Plasmonic Control of Multi-Electron Transfer and C-C Coupling in Visible-Light-Driven $CO_2$ Reduction on Au Nanoparticles. *Nano Lett.* **2018**, *18*, 2189−2194.
(85) Yu, S.; Jain, K. P. Selective Branching of Plasmonic Photosynthesis into Hydrocarbon Production and Hydrogen Generation. *ACS Energy Lett.* **2019**, *4*, 2295−2300.
(86) Cui, X.; Wang, J.; Liu, B.; Ling, S.; Long, R.; Xiong, Y. Turning Au Nanoclusters Catalytically Active for Visible-Light-Driven $CO_2$ Reduction through Bridging Ligands. *J. Am. Chem. Soc.* **2018**, *140*, 16514−16520.
(87) Kumari, G.; Zhang, X.; Devasia, D.; Heo, J.; Jain, K. P. Watching Visible Light-Driven $CO_2$ Reduction on a Plasmonic Nanoparticle Catalyst. *ACS Nano* **2018**, *12*, 8330−8340.




https://doi.org/10.1021/acsnano.2c10470
*ACS Nano* 2023, 17, 4526−4538